

## A NEW NON-PARAMETRIC METHOD TO INFER GALAXY CLUSTER MASSES FROM WEAK LENSING

TOBIAS MISTELE<sup>1</sup>, AMEL DURAKOVIC<sup>2,3</sup><sup>1</sup>Department of Astronomy, Case Western Reserve University, 10900 Euclid Avenue, Cleveland, Ohio 44106, USA<sup>2</sup>CEICO — FZU, Institute of Physics of the Czech Academy of Sciences, Na Slovance 1999/2, 182 00 Prague 8, Czechia<sup>3</sup>Université de Strasbourg, CNRS, Observatoire astronomique de Strasbourg, UMR 7550, 11 Rue de l'Université, 67000 Strasbourg, France*Version August 27, 2024*

## ABSTRACT

We introduce a new, non-parametric method to infer deprojected 3D mass profiles  $M(r)$  of galaxy clusters from weak gravitational lensing observations. The method assumes spherical symmetry and a moderately small convergence,  $\kappa \lesssim 1$ . The assumption of spherical symmetry is an important restriction, which is, however, quite common in practice, for example in methods that fit lensing data to an NFW profile. Unlike other methods, our method relies on spherical symmetry only at radii larger than the radius  $r$  at which the mass  $M$  is inferred. That is, the method works even if there is a non-symmetric inner region. We provide an efficient implementation in Julia code that runs in a few milliseconds per galaxy cluster. We explicitly demonstrate the method by using data from KiDS DR4 to infer mass profiles for two example clusters, Abell 1835 and Abell 2744, finding results consistent with existing literature.

## 1. INTRODUCTION

Both strong and weak gravitational lensing are powerful tools to infer the dynamical masses of galaxy clusters (e.g. Bartelmann & Schneider 2001; Umetsu 2020; Normann et al. 2024). A common procedure is to fit a parametric, spherically symmetric mass profile such as an NFW profile (Navarro et al. 1996) to lensing observations (e.g. Euclid Collaboration et al. 2024a; Medezinski et al. 2016; Applegate et al. 2014).

Here, we introduce a new method to infer deprojected 3D masses of galaxy clusters from weak gravitational lensing observations. This method is based on the deprojection formula from Mistele et al. (2024b) which was originally developed for galaxy-galaxy lensing assuming that the convergence  $\kappa$  is negligible,  $\kappa \ll 1$ . We adapt this method to the case with moderate values of  $\kappa$  (which we denote as  $\kappa \lesssim 1$ ) so that it can be applied to galaxy clusters, at least outside the central strong lensing regions. This method assumes spherical symmetry but does not assume a specific form of the mass profile, i.e. it is a non-parametric method. Importantly, it is straightforward to implement and computationally efficient.

The assumption of spherical symmetry is an important restriction. We note, however, that this assumption is quite common in practice, for example in methods that fit lensing data to a spherically symmetric mass profile (e.g. Euclid Collaboration et al. 2024a; Medezinski et al. 2016; Applegate et al. 2014). Further, as we will see below, when inferring the deprojected mass at a spherical radius  $r$  our method does not require spherical symmetry at radii smaller than  $r$ . Thus, unlike some other methods (e.g. Sommer et al. 2022), our method works even for clusters with a non-symmetric inner region.

We describe our new method in Sec. 2, demonstrate

and illustrate it with two explicit example clusters in Sec. 3, and conclude in Sec. 4.

## 2. THE METHOD

Our new method is based on a deprojection formula from Mistele et al. (2024b) that allows us to convert excess surface density (ESD) profiles  $\Delta\Sigma(R)$  (see below) into deprojected mass profiles  $M(r)$  assuming spherical symmetry (see also Mistele et al. 2024a). For galaxy-galaxy lensing, which is what was considered in Mistele et al. (2024b),  $\Delta\Sigma$  is typically straightforward to measure because the convergence  $\kappa$  is negligible (Bartelmann & Schneider 2001). For galaxy clusters, however,  $\kappa$  is not necessarily small. Thus, an extra step is needed to infer  $\Delta\Sigma$  from observations. This extra step is the main subject of this section.

## 2.1. Main theoretical result

Weak lensing observations are based on the (complex) ellipticities  $\epsilon_s$  of a large number of source galaxies  $s$  behind a lens  $l$ . These give an estimate of the (complex) reduced shear  $g$  around the lens,

$$g = \frac{\gamma}{1 - \kappa}, \quad (1)$$

where  $\gamma$  is the (complex) shear and  $\kappa$  is the convergence (Bartelmann & Schneider 2001). The convergence is given by  $\Sigma/\Sigma_{\text{crit},ls}$  where  $\Sigma$  is the surface density of the lens and  $\Sigma_{\text{crit},ls}$  is the critical surface density,

$$\Sigma_{\text{crit},ls}^{-1} = \frac{4\pi G_N}{c^2} \frac{D(z_l)D(z_l, z_s)}{D(z_s)}, \quad (2)$$

with the Newtonian gravitational constant  $G_N$  and the angular diameter distances to the lens,  $D(z_l)$ , to the

source,  $D(z_s)$ , and between the source and the lens  $D(z_l, z_s)$ .

The tangential component  $\gamma_+$  of  $\gamma$ , and therefore also the tangential component  $g_+$  of  $g$ , is closely related to the ESD profile  $\Delta\Sigma(R)$  (see below) that we need in order to use the results from Mistlele et al. (2024b). Indeed, multiplying  $\gamma_+$  by the critical surface density and averaging azimuthally gives  $\Delta\Sigma$  (e.g. Kaiser & Squires 1993).

Thus, we consider the azimuthal average of the tangential reduced shear  $g_+$  times the critical surface density,

$$G_+(R) \equiv \langle \Sigma_{\text{crit},ls} \cdot g_+ \rangle(R) = \frac{\sum_s W_{ls} \cdot \Sigma_{\text{crit},ls} \epsilon_{+,ls}}{\sum_s W_{ls}}, \quad (3)$$

where the  $W_{ls}$  are weights (see Sec. 3.1) and  $\epsilon_{+,ls}$  denotes the tangential ellipticity of the source  $s$  with respect to the lens  $l$ . The sum in Eq. (3) runs over all sources at a given projected distance  $R$  from the lens.

We now assume that the lens is spherically symmetric. Then, the quantity  $G_+(R)$  is related to the surface density  $\Sigma(R)$  and the ESD profile  $\Delta\Sigma(R)$  of the lens by (Seitz & Schneider 1997; Umetsu 2020),

$$G_+(R) \simeq \frac{\Delta\Sigma(R)}{1 - f_c(R)\Sigma(R)}, \quad (4)$$

where the "≈" indicates that this relation is valid only as long as  $f_c \cdot \Sigma$  is not too large (Seitz & Schneider 1997) and  $f_c$  is the average inverse critical surface density,

$$f_c(R) \equiv \langle \Sigma_{\text{crit},ls}^{-1} \rangle(R), \quad (5)$$

As in Eq. (3), the average runs over the sources at a projected distance  $R$  and uses weights  $W_{ls}$ . In the following, we assume that  $f_c \cdot \Sigma$  is indeed not too large so that Eq. (4) is valid. We denote this condition by

$f_c(R)\Sigma(R) \lesssim 1$  which is roughly equivalent to

$$\kappa = \Sigma/\Sigma_{\text{crit}} \lesssim 1. \quad (6)$$

Finally, the ESD profile  $\Delta\Sigma$  is defined in terms of the surface density  $\Sigma$ ,

$$\Delta\Sigma(R) \equiv \frac{2}{R^2} \int_0^R dR' R' \Sigma(R') - \Sigma(R). \quad (7)$$

Both  $G_+$  and  $f_c$  are observational quantities that can be measured directly. Our goal is to infer the deprojected mass of the lens, given these two quantities. To achieve this, we will use the relation Eq. (4) as well as previous results from Mistlele et al. (2024b). We also make the mild additional assumption that the mass density  $\rho$  of the lens asymptotically falls off faster than  $1/r$ .

Our strategy is as follows. First, we eliminate  $\Sigma$  from Eq. (4) by using the following relation between  $\Sigma$  and  $\Delta\Sigma$  which follows from Eq. (7) (Mistlele et al. 2024b),

$$\Sigma(R) = -\Delta\Sigma(R) + \int_R^\infty dR' \frac{2\Delta\Sigma(R')}{R'}. \quad (8)$$

This gives a relation between the observational quantities  $G_+$  and  $f_c$  on the one hand and  $\Delta\Sigma$  on the other hand, with no more dependence on  $\Sigma$ . The next step is to solve this relation for  $\Delta\Sigma$  which gives  $\Delta\Sigma$  as a function of  $G_+$  and  $f_c$ . Finally, we use the deprojection formula from Mistlele et al. (2024b) which, given  $\Delta\Sigma$ , allows us to calculate the dynamical deprojected mass  $M(r)$  within a spherical radius  $r$ .

Details of this derivation are given in Appendix A. The final result is

$$\frac{M(r)}{r^2} = 4 \int_0^{\pi/2} d\theta \Delta\Sigma\left(\frac{r}{\sin\theta}\right), \quad (9)$$

which is the deprojection formula from Mistlele et al. (2024b), with the following specific  $\Delta\Sigma$ ,

$$\Delta\Sigma(R) = \frac{1}{f_c(R)} \frac{G_+ f_c(R)}{1 - G_+ f_c(R)} \left[ 1 - \int_R^\infty dR'' \frac{f_c(R)}{f_c(R'')} \frac{2}{R''} \frac{G_+ f_c(R'')}{1 - G_+ f_c(R'')} \exp\left(-\int_R^{R''} dR' \frac{2}{R'} \frac{G_+ f_c(R')}{1 - G_+ f_c(R')}\right) \right], \quad (10)$$

where we introduced the shorthand notation  $G_+ f_c(R) \equiv G_+(R) \cdot f_c(R)$ . This allows us to calculate the dynamical mass  $M(r)$  from the observational quantities  $G_+$  and  $f_c$ . Thus, Eq. (10) together with Eq. (9) is the core theoret-

ical result of this work.

In practice, the average inverse critical surface density  $f_c(R)$  is often approximately constant as a function of  $R$ , i.e.  $f_c(R) \approx \text{const}$ . In this case, Eq. (10) simplifies,

$$\Delta\Sigma(R)|_{f_c=\text{const}} = \frac{1}{f_c} \frac{G_+ f_c(R)}{1 - G_+ f_c(R)} \exp\left(-\int_R^\infty dR' \frac{2}{R'} \frac{G_+ f_c(R')}{1 - G_+ f_c(R')}\right). \quad (11)$$

In the limit  $\kappa \ll 1$ , the relation between  $\Delta\Sigma$  and the observational quantities  $G_+$  and  $f_c$  becomes even simpler, namely  $\Delta\Sigma(R) \approx G_+(R)$ . This last relation is what the galaxy-galaxy lensing analysis in Mistlele et al. (2024b)

is based on.

The above assumes that an estimate of  $\Sigma_{\text{crit},ls}$  is available for each individual source  $s$ . If this is not the case and only ensemble information is available, we can still

use Eq. (9) and Eq. (10) to estimate the deprojected mass profile  $M(r)$ , if we adapt the definitions of  $G_+$  and  $f_c$ ,

$$G_+ = \langle \Sigma_{\text{crit},ls} g_+ \rangle \rightarrow G_+ = \frac{\langle g_+ \rangle}{\langle \Sigma_{\text{crit},ls}^{-1} \rangle}, \quad (12a)$$

$$f_c = \langle \Sigma_{\text{crit},ls}^{-1} \rangle \rightarrow f_c = \frac{\langle \Sigma_{\text{crit},ls}^{-2} \rangle}{\langle \Sigma_{\text{crit},ls}^{-1} \rangle}. \quad (12b)$$

This can be seen by retracing the above derivation with Eq. (4) replaced by the analogous relation (Umetsu 2020; Applegate et al. 2014; Seitz & Schneider 1997)

$$\frac{\langle g_+ \rangle}{\langle \Sigma_{\text{crit},ls}^{-1} \rangle} \simeq \frac{\Delta \Sigma}{1 - \frac{\langle \Sigma_{\text{crit},ls}^{-2} \rangle}{\langle \Sigma_{\text{crit},ls}^{-1} \rangle} \Sigma}, \quad (13)$$

which also holds as long as  $\kappa$  is not too large. In practice, if individual source redshifts are not available, a separate estimate of  $f_c$  for each radius  $R$  is likely also not available. In this case, one may as well use Eq. (11) instead of Eq. (10) to simplify the calculation.

Mathematically, both Eq. (10) and Eq. (11) are only valid as long as  $G_+ f_c(R)$  remains smaller than 1. This roughly corresponds to the condition that the reduced tangential shear  $g_+$  is smaller than 1,  $g_+ < 1$ . In fact, this condition is implicit in weak-lensing results we build on such as Eq. (3). Thus, it is not an important additional restriction; it is mostly just a reminder that we are working within the weak-lensing regime.

From Eq. (10) and Eq. (9) we see that the inferred mass  $M(r)$  at a radius  $r$  depends on observations only from radii  $R$  larger than  $r$ . This is useful in case no data from small radii is available. But perhaps more importantly, it also is the basis for another, more generally useful property of our method.

## 2.2. Spherical symmetry not required at small radii

This property is that our method works even for clusters with a non-symmetric inner region. In particular, the results from the previous subsection hold even when the mass density  $\rho$  of the lens is spherically symmetric only beyond some spherical radius  $r_s$ . That is, Eqs. (10) and (9) still give the correct mass  $M(r)$  at radii  $r$  larger than  $r_s$  even when the lens is not spherically symmetric at radii smaller than  $r_s$ .

To see this, we first note that, at  $R > r_s$ , the observable quantities  $G_+(R)$  and  $f_c(R)$  that enter these equations do not depend on how the mass within the projected radius  $R$  is distributed. They only depend on the cumulative projected mass  $M_{2D}(R)$  within  $R$  and on the projected surface density  $\Sigma(R)$  at  $R$ . This is because Eq. (4) holds at  $R > r_s$  even when  $\rho$  is not spherically symmetric at small radii (Umetsu 2020; Euclid Collaboration et al. 2024a); one just needs to replace the surface density  $\Sigma(R)$  by the azimuthally averaged surface density  $\langle \Sigma \rangle(R)$  in the definition of  $\Delta \Sigma(R)$  Eq. (7).

Next, consider a second lens with the same mass distribution as the original lens, except with all the mass within  $r_s$  collapsed into a single point at the origin. These two lenses produce the exact same observables  $G_+(R)$  and  $f_c(R)$  at  $R > r_s$ . As a consequence, using Eq. (10) and Eq. (9) to infer a mass profile  $M(r)$  for  $r > r_s$  also gives the exact same result for both lenses.

This is because, when inferring the mass  $M$  at  $r$ , Eq. (10) and Eq. (9) only make use of  $G_+$  and  $f_c$  evaluated at radii larger than  $r$ .

Now, for the second lens we know that our method infers the correct mass profile  $M(r)$  because that lens is spherically symmetric everywhere. Further, the two lenses have the same cumulative mass profile  $M(r)$  beyond  $r_s$ . Thus, it follows that our method infers the correct mass profile  $M(r)$  for  $r > r_s$  even when the lens is not spherically symmetric at radii smaller than  $r_s$ .

## 2.3. Practical considerations

To use Eq. (9) and Eq. (10) in practice requires a few additional considerations. For example, the integrals in Eq. (10) extend to  $\infty$  and therefore require  $G_+(R)$  and  $f_c(R)$  at arbitrarily large radii  $R$ . In practice, however, these are measured only up to some finite maximum radius  $R_{\text{max}}$ . To deal with this, we extrapolate  $G_+(R)$  and  $f_c(R)$  beyond  $R_{\text{max}}$  using a simple power law for  $G_+$  and a constant for  $f_c$ ,

$$G_+(R > R_{\text{max}}) \equiv G_+(R_{\text{max}}) \cdot \left( \frac{R_{\text{max}}}{R} \right)^n, \quad (14a)$$

$$f_c(R > R_{\text{max}}) \equiv f_c(R_{\text{max}}). \quad (14b)$$

This extrapolation is an important systematic uncertainty. However, in practice, it becomes important only close to the last measured data point at  $R = R_{\text{max}}$ . Over most of the radial range, the extrapolation has little impact on the inferred mass  $M(r)$  (see Sec. 3 below). This is because most of the signal in the inferred  $M(r)$  comes from  $G_+(R)$  and  $f_c(R)$  at  $R \sim r$ .

For our explicit examples below, we extrapolate assuming  $n = 1$  which corresponds to a singular isothermal sphere. We take the uncertainty in this choice into account as a systematic error. In particular, we adopt the difference between extrapolation with  $n = 1/2$  and  $n = 2$  as a systematic error. Schematically,

$$\sigma_{M(r)}|_{\text{syst}}^{\text{extrapolate}} \equiv \left| M(r)|^{n=2} - M(r)|^{n=1/2} \right|. \quad (15)$$

For comparison,  $n = 2$  corresponds to  $G_+$  asymptotically dropping off as for a point mass. For  $n = 1/2$ ,  $G_+$  drops off slower than for a singular isothermal sphere. These two extreme cases likely bracket the true behavior of  $G_+$ .

Similarly,  $G_+$  and  $f_c$  are measured in discrete radial bins but the continuous integrals in Eq. (10) require them at all radii. Thus, we interpolate between the discrete radial bins. For our explicit examples below we use linear interpolation and we adopt the difference between linear and quadratic interpolation as an estimate of the systematic error due to interpolation. Schematically,

$$\sigma_{M(r)}|_{\text{syst}}^{\text{interpolate}} \equiv \left| M(r)|^{\text{quadratic}} - M(r)|^{\text{linear}} \right|. \quad (16)$$

We interpolate linearly (or quadratically) in  $R$ . Another reasonable option is to interpolate in  $\ln R$ . For our explicit examples below, this choice does not make a significant difference.

For the statistical uncertainties and covariances, we use linear error propagation to convert uncertainties on  $G_+$  into uncertainties and covariances on the inferred mass  $M$ . Linear error propagation requires calculating the Jacobian of the inferred mass  $M(r)$  understood as a func-

tion of the measured values  $G_+(R_i)$  where  $R_i$  denote the discrete radii where  $G_+$  is measured. This calculation is cumbersome to do by hand. To avoid this, we wrote differentiable numerical Julia code to evaluate Eq. (10) and Eq. (9). Differentiable here means that the Julia package ‘ForwardDiff.jl’ (Revels et al. 2016) can automatically calculate the needed Jacobians for us. Linear error propagation then reduces to a simple matrix multiplication. Our code is publicly available<sup>1</sup> and takes only a few milliseconds per galaxy cluster to run on a standard personal computer. In Appendix B, we discuss how we efficiently evaluate the integrals in Eq. (9) and Eq. (10).

### 3. EXPLICIT EXAMPLES

We now demonstrate our method explicitly using two example galaxy clusters listed in the LC2 catalog (Sereno 2015), Abell 1835 and Abell 2744. Abell 2744 is a merging system for which our assumption of spherical symmetry is likely not a good approximation. It is, however, still useful to compare the results of our method to the results of other methods that also assume spherical symmetry such as the single-halo model from Medezinski et al. (2016).

We use weak-lensing data from KiDS DR4 (Kuijken et al. 2019; Giblin et al. 2021). We select Abell 1835 and Abell 2744 because they are massive clusters with a relatively high source galaxy number density in KiDS. This gives a reasonable signal-to-noise ratio. As we will see, our new method gives results compatible with previous mass measurements from Applegate et al. (2014) and Medezinski et al. (2016). Our uncertainties are larger, however, because we make fewer assumptions about the mass profiles of the lenses and because the source galaxy samples used in Applegate et al. (2014) and Medezinski et al. (2016) have significantly higher number densities compared to KiDS.

#### 3.1. Data

We mostly follow the procedure of Mistele et al. (2024b) and Brouwer et al. (2021). In particular, we use ellipticities from the KiDS-1000 SOM-gold source galaxy catalog (Kuijken et al. 2019; Wright et al. 2020; Giblin et al. 2021; Hildebrandt et al. 2021) to estimate  $G_+$  according to Eq. (3), with weights  $W_{ls} = w_s \Sigma_{\text{crit},ls}^{-2}$  where  $w_s$  estimates the precision of the ellipticity measurement of the source  $s$  (Brouwer et al. 2021; Giblin et al. 2021). We handle multiplicative and additive biases of the ellipticities as well as their statistical uncertainties as in Mistele et al. (2024b).

To minimize contamination, we apply the *griz*<sup>2</sup> color-color cuts proposed in Euclid Collaboration et al. (2024c, Table A.1) and restrict the sources to those satisfying  $z_B > z_l + \Delta z$  where  $z_B$  is the photometric redshift of the source,  $z_l$  is the redshift of the lens, and  $\Delta z = 0.1$ .

We calculate the critical surface densities  $\Sigma_{\text{crit},ls}$  following the procedure of Dvornik et al. (2017); Brouwer et al. (2021) to take into account uncertainties in the

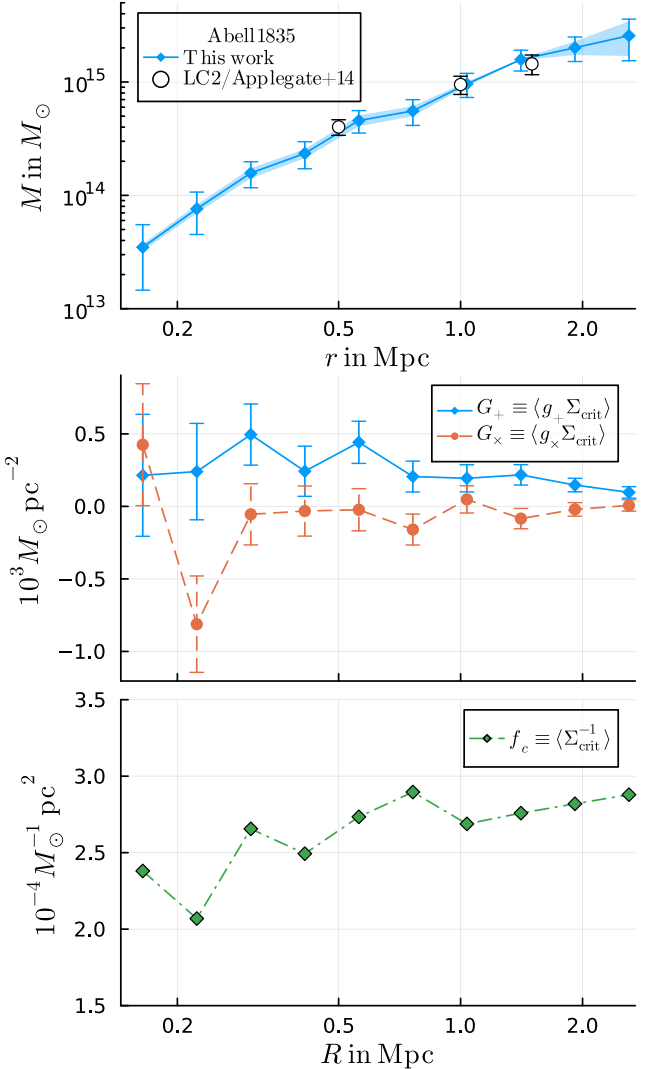


FIG. 1.— *Top*: The deprojected spherical mass  $M(r)$  of Abell 1835 inferred using our new method described in Sec. 2 (blue symbols). Error bars indicate the statistical uncertainty. The colored error band indicates the systematic uncertainties from extrapolating beyond the last data point and interpolating between the discrete data points (see Sec. 2.3). For comparison, white symbols show mass estimates from Applegate et al. (2014), obtained using different data and a different method. Our statistical uncertainties are larger because we make fewer assumptions about the mass profile and because the KiDS data we use has a smaller source number density. *Middle*: The observed tangential reduced shear  $G_+ = \langle g_+ \Sigma_{\text{crit}} \rangle$  and the corresponding cross component  $G_x$ . The cross component  $G_x$  is consistent with zero, as it should be. *Bottom*: The observed average inverse critical surface density  $f_c = \langle \Sigma_{\text{crit}}^{-1} \rangle$ . The observational quantities  $G_+$ ,  $G_x$ , and  $f_c$  are inferred from KiDS DR4 data.  $G_+$  and  $f_c$  enter the calculation of  $M$  through Eq. (10) and Eq. (9).

source redshifts,

$$\Sigma_{\text{crit},ls}^{-1} = \frac{4\pi G}{c^2} D(z_l) \int_{z_l}^{\infty} dz_s n_{ls}(z_s) \cdot \frac{D(z_l, z_s)}{D(z_s)}. \quad (17)$$

The function  $n_{ls}(z)$  is determined as follows. For a given  $z_l$  and a given photometric source redshift  $z_{B,s}$ , we check in which of the five tomographic bins from Hildebrandt et al. (2021) the  $z_{B,s}$  value belongs, get the corresponding redshift distribution function from Hildebrandt et al.

<sup>1</sup> <https://github.com/tmistele/SphericalClusterMass.jl>

<sup>2</sup> KiDS provides *griz* but not *z*. To deal with this, we replace *z* with *Z*, which KiDS does provide, and, for simplicity, ignore the small difference between *z* and *Z* (Hewett et al. 2006).

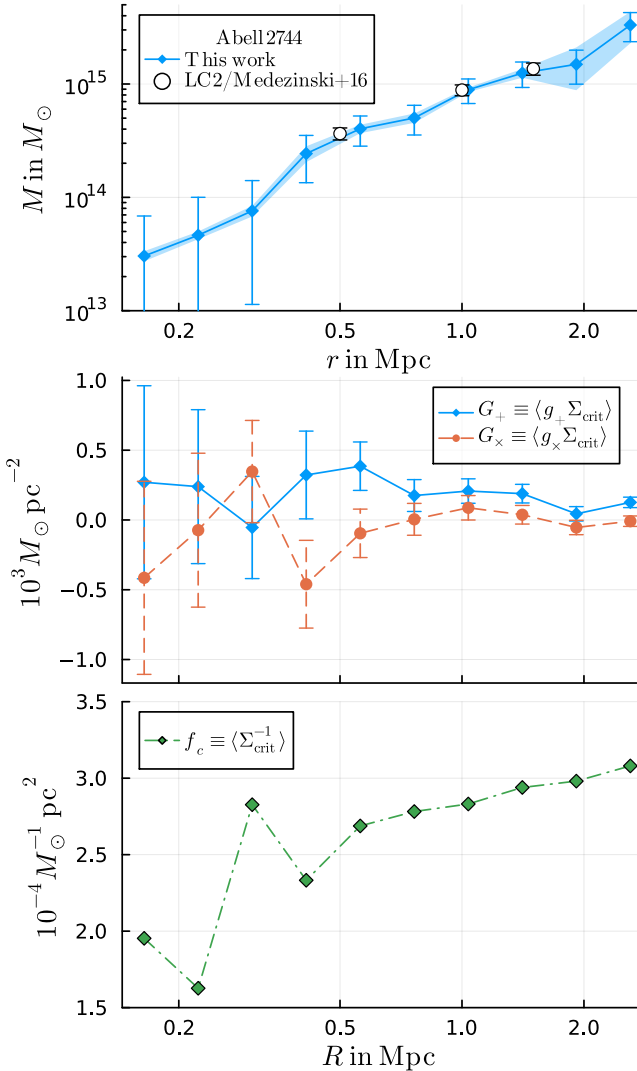


FIG. 2.— Same as Fig. 1 but for Abell 2744. White symbols in the top panel show mass estimates from Medezinski et al. (2016).

(2021), and normalize this distribution to unity in the interval  $[z_l, \infty)$ .

We take cluster coordinates and redshifts from the LC2 catalog. For compatibility with LC2, we assume a flat FLRW cosmology with  $H_0 = 70 \text{ km s}^{-1} \text{ Mpc}^{-1}$  and  $\Omega_m = 0.3$ . We use 10 logarithmic radial bins with the largest bin edge being 3 Mpc and with a logarithmic bin width of  $1/7.5$ .

### 3.2. Results

Fig. 1 and Fig. 2 show the inferred deprojected mass profiles  $M(r)$  (top panels) for Abell 1835 and Abell 2744, respectively, and the observed quantities  $G_+(R)$  and  $f_c(R)$  (middle and bottom panels) from which  $M(r)$  is calculated using Eq. (10) and Eq. (9). As a cross-check, the middle panels also show the cross component of the reduced shear, denoted  $G_x$  and defined analogously to Eq. (3), which is consistent with zero, as it should be.

We see that the systematic uncertainties from having to extrapolate and interpolate the observed  $G_+(R)$  and  $f_c(R)$  profiles (see Sec. 2.3) become comparable to the

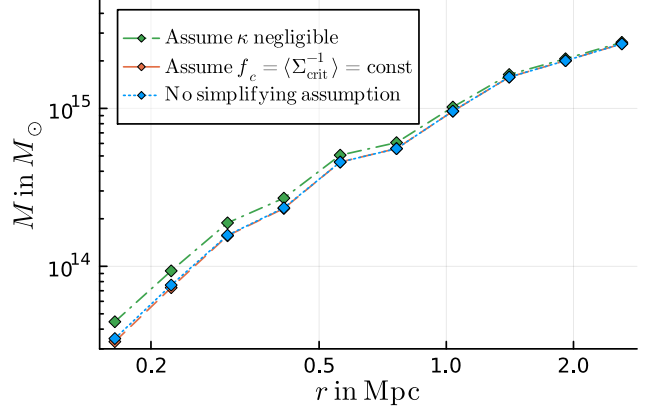


FIG. 3.— The inferred deprojected mass  $M(r)$ , as in Fig. 1, but making use of additional simplifying assumptions. For comparison we also show the original result without these simplifications (dotted blue line). The two simplifying assumptions considered are that the average inverse critical surface density  $f_c = \langle \Sigma_{\text{crit}}^{-1} \rangle$  is approximately constant (dashed red line) and that the convergence  $\kappa$  is negligible (dash-dotted green line). The former allows using the simpler Eq. (11) instead of Eq. (10) to infer  $\Delta\Sigma$  from  $G_+$  and  $f_c$ . The latter corresponds to the even simpler relation  $\Delta\Sigma = G_+$ . For visual clarity, we do not show the uncertainties.

statistical uncertainties only close to the last measured data point. Over most of radial range we probe, these systematics are relatively unimportant. Thus, the inferred masses are free from any assumptions about the mass profile of the lens over most of the radial range.

The uncertainties of our mass estimates are larger than those of Applegate et al. (2014) and Medezinski et al. (2016). This may be in part due to the fact that we make fewer assumptions about the mass profile of the lens. But another important part is that the number density of source galaxies in KiDS DR4 is much smaller than the source number densities in Applegate et al. (2014) and Medezinski et al. (2016). Indeed, our sample of source galaxies has an average number density of  $3.9 \text{ arcmin}^{-2}$  for Abell 1835 and  $4.6 \text{ arcmin}^{-2}$  for Abell 2744, while the source galaxies used in Applegate et al. (2014) and Medezinski et al. (2016) have much larger densities of about  $20 \text{ arcmin}^{-2}$  and  $10 \text{ arcmin}^{-2}$ , respectively. Thus, despite making fewer assumptions, we expect that our method would give uncertainties much closer to those of Applegate et al. (2014) and Medezinski et al. (2016) when applied to the same underlying data.

As discussed in Sec. 2.1, Eq. (10) simplifies if the average inverse critical surface density  $f_c(R)$  is constant. Fig. 1 and Fig. 2 show that  $f_c$  is indeed reasonably constant.<sup>3</sup> Thus, we repeat our analysis for Abell 1835 using the simplified formula Eq. (11) which assumes that  $f_c$  is constant. In particular, we take the constant value of  $f_c$  to be the value of  $f_c(R)$  calculated in a single radial bin that spans the whole radial range we consider. Fig. 3 shows that this does not significantly affect the inferred mass  $M(r)$ . Thus, the simplifying assumption of a con-

<sup>3</sup> Fig. 1 and Fig. 2 also show that  $f_c$  is not perfectly constant, with a slight downward trend at small radii. One potential cause is residual contamination from cluster members. Another is obscuration, which affects high-redshift sources more than low-redshift ones (e.g. Kleinebreil et al. 2024, Fig. 7). This will be further investigated in future work.

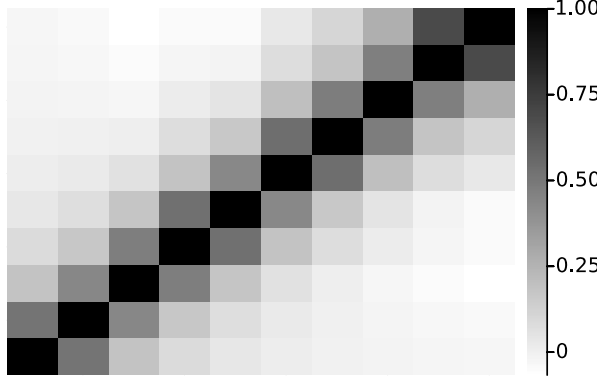


FIG. 4.— The correlation matrix of inferred masses  $M$  at different radii  $r$  and  $r'$  for Abell 1835. The correlation matrix is defined in terms of the covariance matrix as  $\text{Cov}(M(r), M(r'))/\sigma_{M(r)}\sigma_{M(r')}$ . Small radii correspond to the lower left corner.

stant  $f_c$  may be justified in practice.

The purpose of Eq. (10) (and the simplified Eq. (11)) is to take into account that the convergence  $\kappa$  is not always negligible in galaxy clusters. To see this effect of a non-zero  $\kappa$ , we also repeat our analysis with the assumption that  $\kappa$  is negligible, i.e. using  $G_+(R) = \Delta\Sigma(R)$  instead of Eq. (10). Fig. 3 shows that there is a small but significant effect at small and intermediate radii, but not at large radii. This is expected since  $\kappa$  becomes less important at large radii.

Due to the integrals in Eq. (10) and Eq. (9), the inferred masses  $M(r)$  at different radii  $r$  are correlated. The correlation matrix for Abell 1835 is shown in Fig. 4. We see that the inferred masses are correlated only over a relatively limited radial range. This is because, as discussed in Sec. 2.1, most of the signal that goes into  $M(r)$  comes from  $G_+(R)$  and  $f_c(R)$  at radii  $R$  relatively close to  $r$ . This is also the reason why the systematic uncertainties from extrapolating beyond the last data point are limited to radii close to the last data point.

### 3.3. Future improvements

The above explicit examples illustrate our new method and demonstrate that it works well. Further improvements are possible. For example, the statistical uncertainties can be significantly reduced by using data with higher source number densities. This may be possible with upcoming surveys such as Euclid (Euclid Collaboration et al. 2024b) or dedicated, targeted observations

such as those used by Applegate et al. (2014); Medezinski et al. (2016) we compared to above.

There are also a number of physical effects we have not yet taken into account. For example, effects from miscentering or residual contamination which may be relevant at small radii. Miscentering may be particularly relevant for stacked analyses of lower-mass clusters (e.g. Rozo et al. 2011).

At large radii, the lensing signal may receive additional contributions from the correlated environment around the galaxy cluster and the assumption of spherical symmetry may be violated. One way to take this into account is to estimate the local environment’s contribution  $\Delta\Sigma_e$  to the ESD profile  $\Delta\Sigma$  (Oguri & Takada 2011; Oguri & Hamana 2011) and use this to calculate, using Eq. (9), the local environment’s contribution  $M_e(r)$  to our inferred mass  $M(r)$ . We can then add this contribution  $M_e(r)$  to our systematic error estimate. Alternatively, we can subtract  $M_e(r)$  from the inferred mass  $M(r)$ , at the cost of making the final subtracted mass more model-dependent.

Similarly, the contributions from the uncorrelated large-scale structure can be taken into account as an additive contribution to the covariance matrix of  $\Delta\Sigma$  (Hoekstra 2003). That covariance can be propagated into the final statistical uncertainties and covariance matrices of the mass inferred from  $\Delta\Sigma$  using Eq. (9). Such improvements will be investigated in future work.

## 4. CONCLUSION

We have introduced a new, non-parametric method to infer galaxy cluster mass profiles from weak lensing, assuming only spherical symmetry. We have demonstrated that this method gives results consistent with other methods and can be computed efficiently.

## ACKNOWLEDGEMENTS

We thank Federico Lelli, Stacy McGaugh, and Pengfei Li for helpful comments and discussions. This work was supported by the DFG (German Research Foundation) – 514562826. AD was supported by the European Regional Development Fund and the Czech Ministry of Education, Youth and Sports: Project MSCA Fellowship CZ FZU I – CZ.02.01.01/00/22-010/0002906. Based on observations made with ESO Telescopes at the La Silla Paranal Observatory under programme IDs 177.A-3016, 177.A-3017, 177.A-3018 and 179.A-2004, and on data products produced by the KiDS consortium. The KiDS production team acknowledges support from: Deutsche Forschungsgemeinschaft, ERC, NOVA and NWO-M grants; Target; the University of Padova, and the University Federico II (Naples).

## REFERENCES

Applegate D. E., et al., 2014, *MNRAS*, 439, 48  
 Bartelmann M., Schneider P., 2001, *Phys. Rep.*, 340, 291  
 Brouwer M. M., et al., 2021, *A&A*, 650, A113  
 Dvornik A., et al., 2017, *MNRAS*, 468, 3251  
 Euclid Collaboration et al., 2024a, *arXiv e-prints*, p. arXiv:2404.08036  
 Euclid Collaboration et al., 2024b, *arXiv e-prints*, p. arXiv:2405.13491  
 Euclid Collaboration et al., 2024c, *A&A*, 684, A139  
 Giblin B., et al., 2021, *A&A*, 645, A105  
 Hewett P. C., Warren S. J., Leggett S. K., Hodgkin S. T., 2006, *MNRAS*, 367, 454  
 Hildebrandt H., et al., 2021, *A&A*, 647, A124  
 Hoekstra H., 2003, *MNRAS*, 339, 1155  
 Kaiser N., Squires G., 1993, *ApJ*, 404, 441  
 Kleinebreil F., et al., 2024, *arXiv e-prints*, p. arXiv:2402.08456  
 Kuijken K., et al., 2019, *A&A*, 625, A2  
 Medezinski E., Umetsu K., Okabe N., Nonino M., Molnar S., Massey R., Dupke R., Merten J., 2016, *ApJ*, 817, 24  
 Mistele T., McGaugh S., Lelli F., Schombert J., Li P., 2024a, *ApJ*, 969, L3

Mistele T., McGaugh S., Lelli F., Schombert J., Li P., 2024b, *J. Cosmology Astropart. Phys.*, 2024, 020

Navarro J. F., Frenk C. S., White S. D. M., 1996, *ApJ*, 462, 563

Normann B. D., Solevåg-Hoti K., Schaathun H. G., 2024, *arXiv e-prints*, p. arXiv:2405.18930

Oguri M., Hamana T., 2011, *MNRAS*, 414, 1851

Oguri M., Takada M., 2011, *Phys. Rev. D*, 83, 023008

Rackauckas C., Nie Q., 2017, *Journal of Open Research Software*, 5, 15

Revels J., Lubin M., Papamarkou T., 2016, arXiv:1607.07892 [cs.MS]

Rozo E., Rykoff E., Koester B., Nord B., Wu H.-Y., Evrard A., Wechsler R., 2011, *ApJ*, 740, 53

Seitz C., Schneider P., 1997, *A&A*, 318, 687

Sereno M., 2015, *MNRAS*, 450, 3665

Sommer M. W., Schrabback T., Applegate D. E., Hilbert S., Ansarinejad B., Floyd B., Grandis S., 2022, *MNRAS*, 509, 1127

Umetsu K., 2020, *A&A Rev.*, 28, 7

Wright A. H., Hildebrandt H., van den Busch J. L., Heymans C., 2020, *A&A*, 637, A100

## APPENDIX

### A. DERIVATION OF EQ. (10)

We start with Eq. (4). This is a relation between the quantities  $G_+$  and  $f_c$  that we consider as given on the one hand and  $\Delta\Sigma$  and  $\Sigma$  on the other hand. The idea is to transform this equation into a linear ordinary differential equation (ODE) for  $\Delta\Sigma$  which can be solved analytically. Our first step is to multiply Eq. (4) by  $1 - f_c\Sigma$  and use Eq. (8) to eliminate  $\Sigma$  in favor of  $\Delta\Sigma$ ,

$$G_+(R) \left( 1 + f_c(R)\Delta\Sigma(R) - f_c(R) \int_R^\infty dR' \frac{2\Delta\Sigma(R')}{R'} \right) = \Delta\Sigma(R). \quad (\text{A1})$$

Rearranging, we get

$$\Delta\Sigma(R) \left( 1 - \frac{1}{G_+ f_c(R)} \right) - \int_R^\infty dR' \frac{2\Delta\Sigma(R')}{R'} = -\frac{1}{f_c(R)}. \quad (\text{A2})$$

This turns into a linear ODE in  $\Delta\Sigma$  after taking a derivative with respect to  $R$ . This ODE can be written as

$$\Delta\Sigma'(R) + \Delta\Sigma(R) \left[ \frac{2}{H(R)R} + \partial_R \ln(-H(R)) \right] = -\frac{1}{H(R)} \partial_R \frac{1}{f_c(R)}, \quad (\text{A3})$$

with

$$H(R) \equiv 1 - \frac{1}{G_+ f_c(R)}. \quad (\text{A4})$$

The general solution of Eq. (A3) is

$$\Delta\Sigma(R) = E(R) \cdot \left[ \frac{C_0}{H(R_0)} + \int_R^{R_0} dR'' \frac{1}{H(R'')} \left( \partial_{R''} \frac{1}{f_c(R'')} \right) \frac{1}{E(R'')} \right], \quad (\text{A5})$$

where  $C_0$  is an integration constant,  $R_0$  is an auxiliary radius, and the function  $E(R)$  is defined as

$$E(R) \equiv \exp \left( \int_R^{R_0} dR' \left( \frac{2}{H(R')R'} + \partial_{R'} \ln(-H(R')) \right) \right). \quad (\text{A6})$$

We can evaluate the integral over the derivative of the logarithm in  $E(R)$ ,

$$E(R) = \frac{H(R_0)}{H(R)} \exp \left( \int_R^{R_0} \frac{dR'}{R'} \frac{2}{H(R')} \right). \quad (\text{A7})$$

Putting this back into Eq. (A5) then gives

$$\Delta\Sigma(R) = \frac{1}{H(R)} \exp \left( \int_R^{R_0} \frac{dR'}{R'} \frac{2}{H(R')} \right) \cdot \left[ C_0 + \int_R^{R_0} dR'' \left( \partial_{R''} \frac{1}{f_c(R'')} \right) \exp \left( - \int_{R''}^{R_0} \frac{dR'}{R'} \frac{2}{H(R')} \right) \right]. \quad (\text{A8})$$

We can replace  $R_0$  with  $\infty$  by absorbing some constant terms into the integration constant  $C_0$ ,

$$\Delta\Sigma(R) = \frac{1}{H(R)} \exp \left( \int_R^\infty \frac{dR'}{R'} \frac{2}{H(R')} \right) \cdot \left[ C_0 + \int_R^\infty dR'' \left( \partial_{R''} \frac{1}{f_c(R'')} \right) \exp \left( - \int_{R''}^\infty \frac{dR'}{R'} \frac{2}{H(R')} \right) \right]. \quad (\text{A9})$$

This expression contains a derivative of the observational quantity  $f_c(R)$  which, in practice, can be hard to reliably estimate. To avoid this numerical derivative, we integrate by parts and absorb some more constants into  $C_0$ ,

$$\Delta\Sigma(R) = \frac{1}{H(R)} \left[ C_0 \exp \left( \int_R^\infty \frac{dR'}{R'} \frac{2}{H(R')} \right) - \frac{1}{f(R)} - \int_R^\infty dR'' \frac{1}{f_c(R'')} \frac{2}{R''} \frac{1}{H(R'')} \exp \left( \int_R^{R''} \frac{dR'}{R'} \frac{2}{H(R')} \right) \right]. \quad (\text{A10})$$

It remains to fix this integration constant. To do this, we use our assumption that the mass density of the lens falls off faster than  $1/r$  at  $r \rightarrow \infty$ . We also assume that  $f_c$  stays roughly constant. These assumptions together with the original Eq. (4) imply

$$\lim_{R \rightarrow \infty} \frac{\Delta\Sigma(R)}{G_+(R)} = 1, \quad (\text{A11})$$

and Eq. (A10) then implies

$$C_0 = 0. \quad (\text{A12})$$

Using  $C_0 = 0$  and the definition of  $H(R)$  from Eq. (A4) in Eq. (A10) then gives the final result Eq. (10).

## B. EFFICIENT NUMERICAL EVALUATION

Using Eq. (9) together with Eq. (10) to infer the mass profile  $M(r)$  from the observational quantities  $G_+(R)$  and  $f_c(R)$  means evaluating a nested triple integral for each  $r$ . Such nested integrals can be expensive to evaluate numerically. Here, we show how to efficiently evaluate this nested triple integral by solving two ODEs and then, for each  $r$ , evaluating only a single integral. Each of these steps can be computed efficiently by standard numerical techniques. To numerically solve ODEs and evaluate integrals we use the Julia packages ‘OrdinaryDiffEq.jl’ (Rackauckas & Nie 2017) and ‘QuadGK.jl’, respectively.

We start by defining the integral

$$I(R) \equiv \int_R^\infty dR' \frac{2}{R'} \frac{G_+ f_c(R')}{1 - G_+ f_c(R')} . \quad (\text{B1})$$

This integral can be calculated at each  $R$  by solving the ODE

$$I'(R) = -\frac{2}{R} \frac{G_+ f_c(R)}{1 - G_+ f_c(R)}, \quad (\text{B2})$$

with the boundary condition

$$I(R_{\max}) = \int_{R_{\max}}^\infty dR' \frac{2}{R'} \frac{G_+ f_c(R')}{1 - G_+ f_c(R')} = -\frac{2}{n} \ln(1 - G_+ f_c(R_{\max})), \quad (\text{B3})$$

which we evaluated analytically using our extrapolation beyond the last data point from Eq. (14). Having solved the ODE for  $I(R)$ , we can write Eq. (10) as

$$\Delta\Sigma(R) = \frac{1}{f_c(R)} \frac{G_+ f_c(R)}{1 - G_+ f_c(R)} \left[ 1 - e^{-I(R)} f_c(R) J(R) \right], \quad (\text{B4})$$

where  $J(R)$  is the integral

$$J(R) \equiv \int_R^\infty dR'' \frac{1}{f_c(R'')} \frac{2}{R''} \frac{G_+ f_c(R'')}{1 - G_+ f_c(R'')} e^{+I(R'')} . \quad (\text{B5})$$

We can evaluate  $J(R)$  analogously to  $I(R)$ . That is, we solve the ODE

$$J'(R) = -\frac{1}{f_c(R)} \frac{2}{R} \frac{G_+ f_c(R)}{1 - G_+ f_c(R)} e^{+I(R)}, \quad (\text{B6})$$

with boundary condition

$$J(R_{\max}) = \int_{R_{\max}}^\infty dR'' \frac{1}{f_c(R'')} \frac{2}{R''} \frac{G_+ f_c(R'')}{1 - G_+ f_c(R'')} e^{+I(R'')} = \frac{1}{f_c(R_{\max})} \left( (1 - G_+ f_c(R_{\max}))^{-\frac{2}{n}} - 1 \right). \quad (\text{B7})$$

Having solved the ODE for  $J(R)$ , we can directly obtain  $\Delta\Sigma(R)$  from Eq. (B4). It then only remains to calculate  $M(r)$  using Eq. (9), i.e. using

$$\frac{M(r)}{r^2} = 4 \int_0^{\pi/2} d\theta \Delta\Sigma \left( \frac{r}{\sin\theta} \right). \quad (\text{B8})$$

We evaluate this integral numerically with  $\Delta\Sigma$  given by Eq. (B4). For  $r/\sin\theta$  smaller than  $R_{\max}$ , we use the numerical ODE solutions discussed above for  $I(R)$  and  $J(R)$  in Eq. (B4). For  $r/\sin\theta$  larger than  $R_{\max}$ , we evaluate  $I(R)$  and  $J(R)$  analytically using our extrapolation from Eq. (14).

As discussed in Sec. 2.3, one may choose to interpolate the discrete  $G_+$  and  $f_c$  data points in either  $R$  or  $\ln R$ . In practice, the numerical procedure discussed so far is likely most suitable when interpolating in  $R$ . When interpolating in  $\ln R$ , it may be more appropriate to consider the integrals  $I$  and  $J$  as functions of  $\ln R$  instead of  $R$  and calculate them by solving ODEs written in terms of  $dI/d\ln R$  and  $dJ/d\ln R$  (instead of Eq. (B2) and Eq. (B6) which are written in terms of  $dI/dR$  and  $dJ/dR$ ). It is straightforward to adapt the above procedure to this case by using  $d/d\ln R = R d/dR$ . The provided Julia code supports interpolation in both  $R$  and  $\ln R$  and automatically uses the corresponding way of calculating  $I$  and  $J$ .